J. Fluid Mech. (2010), *vol.* 643, *pp.* 177–206.
doi:10.1017/S0022112009992023

Sub-Kolmogorov resolution partical image velocimetry measurements of particle-laden forced turbulence

TOMOHIKO TANAKA† AND JOHN K. EATON

Department of Mechanical Engineering, Stanford University, Stanford, CA 94305, USA

(Received 13 May 2008; revised 5 September 2009; accepted 7 September 2009; first published online 5 January 2010)

Previous studies have shown that a dilute dispersion of fine particles can either augment or attenuate the gas-phase turbulent kinetic energy (TKE). However, such turbulence modification is not accurately captured by numerical simulation models. A critical reason is that the models do not incorporate flow distortion occurring at small scales on the order of the particle diameter or the Kolmogorov scale. These scales are too small to be resolved by most experiments and simulations, so the small-scale effects remain poorly understood. The main objective of this study is to investigate experimentally the small-scale turbulence structures that affect the overall turbulence modification to improve understanding and prediction of the macroscopic turbulence modification. A high resolution particle image velocimetry (PIV) system was developed that provided two-dimensional velocity field measurements with a sub-Kolmogorov vector spacing of 60 μm. Measurements of gas-phase isotropic turbulence were performed in the facility developed by Hwang & Eaton (*Exp. Fluids*, vol. 36 (3), 2004*a*, p. 444) in the presence of dispersed 500 μm glass, 250 μm glass or 250 μm polystyrene particles at mass loading ratio up to 0.45. The Reynolds number based on the Taylor microscale was 130 for the unladen case. The TKE was attenuated by up to 25 % in the presence of particles. The high-resolution measurements of the dissipation rate show that changes in the dissipation rate are smaller than changes to the TKE, in contrast to previous underresolved experiments. An analysis of a large set of PIV images allowed calculation of the average turbulence distortion around particles. The measurements also showed strong damping of the TKE and strong augmentation of the dissipation rate in a roughly spherical region surrounding the particles.

Key words: isotropic, particle/fluid flows

1. Introduction

1.1. *Background*

Previous investigations of fine particles dispersed in turbulent gas flows have shown that the addition of particles significantly affects the flow structures. The particle–fluid interactions via the no-slip and impermeability conditions at the particle surfaces modify the whole turbulence flow field in a complex manner. The modification of the carrier-phase turbulence properties affects the dispersion of particles, a classic example of two-way coupling.

† Present address: Central Research Laboratory, Hitachi Ltd., 1-280 Higashi-Koigakubo, Kokubunji, Tokyo, 185-8601, Japan. Email address for correspondence: tomohiko.tanaka@stanfordalumni.org

Many experimental studies have reported that particles either augmented or attenuated turbulent kinetic energy (TKE) levels. Experiments in particle-laden flows by Maeda, Hishida & Furutani (1980), Tsuji & Morikawa (1982), Tsuji, Morikawa & Shiomi (1984), Lee & Durst (1982), Kulick, Fessler & Eaton (1994), Sato & Hishida (1996), Sato *et al.* (2000), Paris & Eaton (2001), Kussin & Sommerfeld (2002), Yang & Shy (2005), Benson, Tanaka & Eaton (2005) and Hwang & Eaton (2006) have shown that particles with diameters near the Kolmogorov scale tend to reduce the turbulence level, while particles larger than the Kolmogorov scale are likely to increase the turbulence intensity. Tsuji & Morikawa (1982) examined a particle-laden air flow in a horizontal pipe using laser Doppler velocimetry (LDV). They used 0.2 mm and 3.4 mm plastic particles with mass loading ratios up to 6. They observed attenuation of the streamwise turbulence intensities by the small particles and the augmentation by the large particles. The energy spectrum in the presence of the small particles showed that the spectrum was augmented at high frequencies and attenuated at low frequencies. They concluded that the energy production by the mean shear stress was reduced because of the flattened mean velocity profiles, while the small-scale eddies were disturbed by particles. Similar trends were obtained by Tsuji *et al.* (1984), who extended the study of Tsuji & Morikawa (1982) to a vertical pipe using plastic particles with diameters ranging from 0.2 mm to 3 mm. The strongest attenuation was observed by Kulick *et al.* (1994), who examined fully developed downward turbulence in a channel at $Re_h = 13\,800$ based on the channel half-width using LDV. They used three types of spheres: 50 μm glass, 90 μm glass and 70 μm copper particles with respective St of 11, 35 and 53 at the centreline, and reported attenuation of turbulent kinetic energy by a factor of up to 5 due to the presence of 70 μm copper particles at a mass loading ratio, ϕ, of 0.8. The streamwise velocity energy spectra in the presence of the 70 μm copper particles at the centreline showed a similar trend to Tsuji *et al.* (1984), which was the attenuation at large scales and augmentation at small scales. It is believed that a mechanism of turbulence attenuation is the so-called extra turbulence dissipation due to particles. Large particles that cannot follow the fluid fluctuating velocities exchange forces with the fluid, thereby extracting turbulent kinetic energy from the turbulence. For small particles, the small-scale flow distortions around particles correspond to large velocity gradients. Therefore, the strong distortions increase the viscous dissipation. On the other hand, experiments by Sato & Hishida (1996), Sato *et al.* (2000), Suzuki, Ikenoya & Kasagi (2000) and Kiger & Pan (2002) demonstrated turbulence augmentation by particles. Sato *et al.* (2000) investigated a fully developed particle-laden downward water channel flow at $Re_h = 2870$ in the presence of glass particles with diameters of 189 or 396 μm. They examined the enstrophy evolution equation to investigate the small-scale structure. The positive enstrophy was observed behind the particles induced by wakes, which contributed to the enstrophy production, while the negative value was found in front of particles. They also reported that significant turbulence distortion was observed when the inter-particle spacing was similar to an energy containing eddy scale. An important factor inducing turbulence augmentation is particle wakes. The wake passed by a sphere becomes asymmetric for Reynolds number above 210 and unsteady for Reynolds numbers greater than 270 (Natarajan & Acrivos 1993; Bagchi & Balachandar 2002). Slip velocity created by gravity or the carrier phase acceleration induces energy transfer from the particles to small-scale fluid velocity fluctuations. Such unsteady wakes are a significant source of turbulence augmentation.

In those experiments, there are many parameters such as the particle diameter, Kolmogorov scale, fluid and particle velocity, mass loading ratio and fluid and particle density. The generalization of turbulence modification by particles has been

challenging. Some studies to generalize these turbulence modifications have been attempted. Gore & Crowe (1989) summarized the previous experimental data in pipe and channel turbulence using the ratio of the particle diameter, d_p, and a characteristic turbulence length, l_e. They successfully found a critical ratio of $d_p/l_e = 1/10$ to separate TKE attenuation and augmentation. However, this finding indicates the modification only qualitatively. In order to predict the magnitude of the modulation, a more comprehensive approach is required by considering the other parameters such as the mass loading ratio, ϕ, and particle density, ρ_p. Recently, Eaton (2006) summarized particle-laden flow experiments including homogeneous gas–solid flows, wall-bounded gas–solid flows, free shear flows and liquid–solid flows, and discussed the physical mechanisms by which particles can either augment or attenuate turbulence. It was indicated that the TKE attenuation occurs for particles with Stokes number of $O(1) \sim O(10)$. As Stokes number increases further, the particle wakes cause the TKE augmentation. On the other hand, in solid–liquid two-phase flows with $St \sim O(10^{-1})$, only augmentation of turbulence was reported. Further analysis was done by Tanaka & Eaton (2008). They categorized 30 previous experimental measurements of wall-bounded turbulence conducted by Kiger & Pan (2002), Kulick *et al.* (1994), Kussin & Sommerfeld (2002), Lain, Sommerfeld & Kussin (2002), Lee & Durst (1982), Ljus, Johansson & Almstedt (2002), Sato & Hishida (1996), Suzuki *et al.* (2000), Tsuji & Morikawa (1982) and Tsuji *et al.* (1984) into attenuation and augmentation groups based only on the value of a novel non-dimensional number, Pa. The number defined as $Pa = St\,Re_L^2(\frac{\eta}{L})^3$ was derived using dimensional analysis of the particle-laden Navier–Stokes equations, where η and L are the Kolmogorov length scale and a representative large scale of the turbulence, respectively. Turbulence augmentation occurred for $Pa < 10^3$, where all such cases were solid particles in water. Particles attenuated turbulence for Pa in the range $10^3 < Pa < 10^5$. All of these cases were particle-laden air flows. Further increases in Pa corresponding to air flows laden with large particles resulted in turbulence augmentation. The existence of two critical points suggests that there are two different mechanisms causing turbulence augmentation. At high Pa, augmentation is caused by superposition of laminar-like wakes or even turbulent wakes of individual particles. Yang & Shy (2005) suggested that preferential particle concentration around intense vortical structures may also cause augmentation. This mechanism could be active at low Pa.

Many numerical simulations for particle-laden flows (Squires & Eaton 1990; Elghobashi & Truesdell 1993; Maxey *et al.* 1997; Boivin, Simonin & Squires 1998; Druzhinin & Elghobashi 1999; Sundaram & Collins 1999; Boivin, Simonin & Squires 2000; Druzhinin 2001; Yamamoto *et al.* 2001; Ferrante & Elghobashi 2003; Segura, Eaton & Oefelein 2004) have also been performed to predict and understand the turbulence modification by particles. Squires & Eaton (1990) conducted a direct numerical simulation (DNS) of particle-laden stationary homogeneous and isotropic turbulence in the two-way coupling regime. They used the point–force momentum coupling method in which particles were assumed to be points with no volume. The authors found that light particles increased the energy and dissipation at high wavenumbers, while the dissipation spectrum was attenuated at low wavenumbers due to preferential concentration. Preferential concentration occurs when particle time constants are comparable with the time scale of the turbulence eddy where the particles are swept out of vortex cores and converge into the concentrated space (Squires & Eaton 1991). Preferential sweeping produces significant anisotropy of turbulence and reduces the decay rate of turbulent kinetic energy (Ferrante & Elghobashi 2003). Preferential concentration may mostly affect eddies in a specific size range depending on the particle size and the mass loading ratio. Boivin *et al.*

(1998) extended the DNS study of Squires & Eaton (1990) using more calculation grid points and observed similar trends. Yamamoto *et al.* (2001) conducted large eddy simulation (LES) for particle-laden channel flow following the conditions of Kulick *et al.* (1994). Particles were treated by a Lagrangian tracking method including rotation and inter-particle collisions. They captured the flattened particle mean velocity, wall-normal fluctuation velocity and number density profiles in good agreement with the experiments. However, the turbulence attenuation data were not accurately modelled, especially for large St particles. This could be because small-scale distortions around particles are not represented, since particle diameters in most simulations are smaller than the grid resolution. In the experiments by Kulick *et al.* (1994), the particle velocity was slower than the fluid velocity at the centreline. Fukagata *et al.* (2001) and Yamamoto *et al.* (2001) numerically showed that this was caused by the particle collisions and Benson *et al.* (2005) experimentally showed that it was due to the wall roughness by measuring particle-laden channel flow with both a smooth acrylic wall and a wall with prescribed roughness. Recently, fully resolved DNS studies have been conducted to investigate the small-scale turbulence modification around particles. Burton & Eaton (2005) investigated a fully resolved DNS of decaying homogeneous isotropic turbulence (initially, $Re_\lambda = 32$) around a stationary particle ($\eta = 0.45\ d_p$). Radial profiles of the TKE and ε were obtained by volume-averaging in shells and compared with the unladen case. They observed that significant kinetic energy modification (50 %) and enhancement of the TKE dissipation (at least 50 %) due to the no-slip boundary condition were confined to a region inside one radius from the particle surface. Bagchi & Balachandar (2004) investigated small-scale interaction between an isolated spherical particle and isotropic turbulence using DNS. They observed significant TKE modification around particles. Because of the expense of these fully resolved simulations, it was difficult to obtain a large statistical sample of turbulence attenuation, and no cases were run at high enough volume fraction to see significant global attenuation. Also, a review of numerical approaches for particle-laden turbulence was conducted by Crowe, Troutt & Chung (1996). They covered the advantages and disadvantages of most of the numerical methods: two-equation models, LES, DNS and discrete vortex models.

1.2. *Objectives*

Although many experimental and numerical studies have been conducted, it is still difficult to state clearly a well-defined mechanism of turbulence modulation. Therefore, numerical simulations have not been successful in predicting the magnitude of turbulence modification. In order to understand the physics of turbulence modification by particles, highly resolved investigations of particle-laden flows are required.

In this study, small-scale turbulence modulation was experimentally examined in isotropic forced turbulence with a Kolmogorov scale, η, of 110 μm by developing a sub-Kolmogorov scale resolution PIV system with vector spacing, Δx, of 60 μm. Three types of particles, 250 μm polystyrene, 250 μm glass and 500 μm glass spheres, were used. The objective of this study was to investigate the microscopic particle–fluid interaction around a particle. Section 2 presents the experimental facility. In § 3, the high-resolution two-phase measurement system is described in detail. Section 4 describes and interprets the measurement results. Conclusions are given in § 5.

2. Experimental facility

We investigated a particle-laden air flow in nearly homogeneous and isotropic turbulence in a chamber with small mean velocity. The experimental facility was

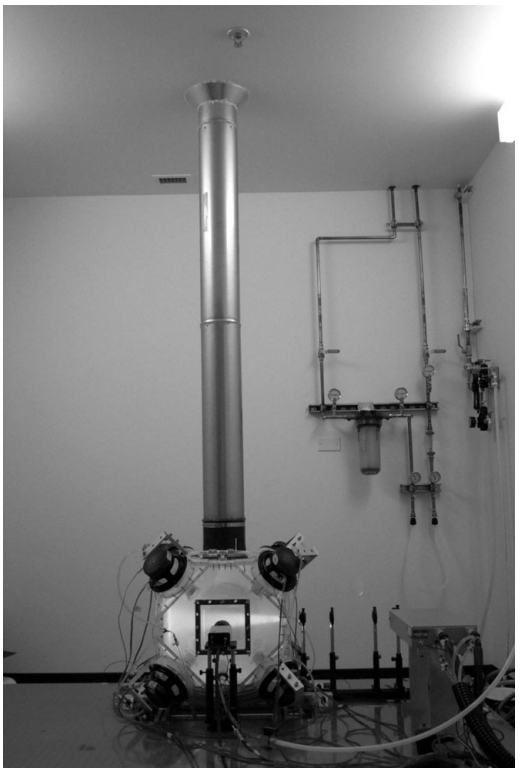

FIGURE 1. Turbulence chamber with the particle feeding chute developed by Hwang & Eaton (2004*a*, *b*). The figure is from Hwang & Eaton (2004*b*).

developed by Hwang & Eaton (2004*a*) and is described in detail in Hwang & Eaton (2004*b*, 2006). A brief description of the facility is given here along with data documenting the specific operating point for the present experiments.

2.1. *Turbulence chamber*

Figure 1 shows the turbulence chamber with the particle feeding chute extending above. Not shown is the particle feeding system which is located on the building's second floor. The test chamber is a cubical Plexiglas box with an inner side of 410 mm and a wall thickness of 12.7 mm. The eight corners are cut off in order to make the box more spherical, where each side of the triangular cutoff area is 193 mm. The corners are covered with triangular plates with attached synthetic jet actuators. The synthetic jets point towards the centre of the chamber so that they generate isotropic turbulence in the centre of the chamber. Each actuator consists of a Pioneer C16EU20-51D cone woofer (165 mm diameter, 60 W RMS, uniform frequency response between 55 and 3 kHz), a 146 mm diameter plenum, a 19 mm diameter round orifice, 40 mm diameter by 74 mm long ejector tube and a turbulence mesh made of galvanized steel woven wire cloth with 1.2 mm diameter wire, 6.4 mm mesh size and 0.34 solidity. The synthetic jet actuators were driven with sine waves each with a random frequency in the range of 90–110 Hz and a random phase using a custom signal source and a Phast PLB-Amp8 8-channel digital amplifier. The woofers were air cooled to maintain the turbulence level constant. The turbulent kinetic energy in the chamber can be varied by changing

RMS velocity in x_1 direction	$\langle u_1^2 \rangle^{1/2}$	($m\,s^{-1}$)	1.05
RMS velocity in x_2 direction	$\langle u_2^2 \rangle^{1/2}$	($m\,s^{-1}$)	0.92
Mean velocity in x_1 direction	$\langle U_1 \rangle$	($m\,s^{-1}$)	–0.04
Mean velocity in x_2 direction	$\langle U_2 \rangle$	($m\,s^{-1}$)	0.14
TKE	$\mathscr{K}$	($m^2\,s^{-2}$)	1.46
TKE dissipation rate	ε	($m^2\,s^{-3}$)	28.2
Kolmogorov microscale	η	(μm)	110
Taylor microscale	λ	(mm)	1.9
Microscale Reynolds number	Re_λ	(–)	127

TABLE 1. Properties of the chamber turbulence.

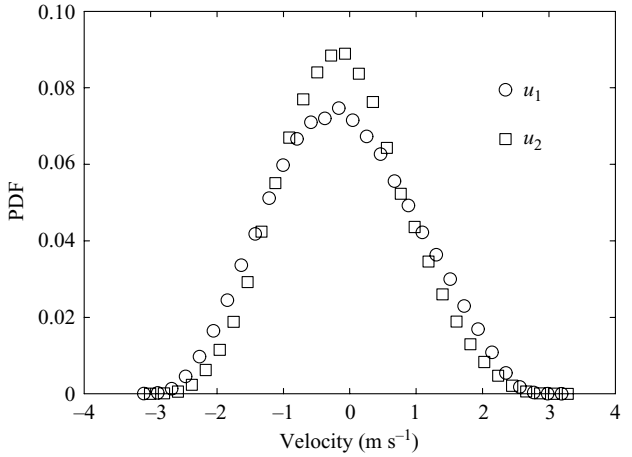

FIGURE 2. PDFs of the velocities u and v for unladen case.

the power supplied to the woofers. The power was monitored and held constant for all experiments reported here.

The turbulence properties are summarized in table 1, and the velocity PDFs for the two measured components are shown in figure 2. All measurements were made using two-dimensional PIV as discussed below. Previous measurements of the third velocity component by Hwang & Eaton (2004*a*) showed that the air turbulence was nearly isotropic, obviating the need for three-dimensional measurements. The mean velocity components are small compared with RMS velocities of 1.05 and 0.92 ($m\,s^{-1}$), where U_i and u_i are instantaneous and fluctuating velocities, respectively. The isotropy ratio ($\langle u_2^2 \rangle^{1/2} / \langle u_1^2 \rangle^{1/2}$) is 0.88. Hwang & Eaton (2004*a*) showed that the RMS velocity components were homogeneous within less than ± 10 % over a 40 mm cube at the centre of the chamber. This region surrounds and includes the smaller measurement volume used for the present experiment. They documented small mean velocity gradients, which may have been a source of turbulent production. However, Hwang & Eaton (2004*a*) measured a shear stress correlation coefficient of only 0.023. This shows that the turbulence generation by mean velocity gradients was very small. Larger mean velocity gradients were induced in the chamber by the particles falling only through the centre of the chamber. This produced an overall mean circulation in the chamber which was not documented quantitatively. As shown later, this flow produced an insignificant fraction of the total turbulent kinetic energy.

	d_p (μm)	ρ_p (kg m^{-3})	τ_p (s)	v_t (m s^{-1})	Re_p	St
Glass	500	2500	0.41	4.0	134	550
Glass	250	2500	0.20	2.0	33	274
Polystyrene	250	1000	0.10	1.0	17	138

TABLE 2. Estimated particle characteristic scales.

By assuming isotropic turbulence, the TKE, $\mathscr{K}$, and the TKE dissipation rate, ε, are estimated as

$$\mathscr{K} = \frac{3}{4}\left(\langle u_1^2\rangle + \langle u_2^2\rangle\right), \tag{2.1}$$

$$\varepsilon = \frac{3}{2}(\varepsilon_{11} + \varepsilon_{22}) + 6\varepsilon_{12}. \tag{2.2}$$

Each component of the dissipation rate is obtained by the definition of $2\nu\langle s_{ij}s_{ij}\rangle$, where s_{ij} is the fluctuating strain rate. The TKE dissipation was obtained by using a correction method introduced by Tanaka & Eaton (2007*a*) in order to eliminate the PIV noise. This is critical for high-resolution PIV as demonstrated by Saarenrinne & Piirto (2000). The correction method is described as

$$\varepsilon \cong \frac{4\varepsilon_m|_{2\Delta x} - \varepsilon_m|_{\Delta x}}{3}, \tag{2.3}$$

where the subscript, m, denotes a quantity obtained from measured PIV data, and $\varepsilon_m|_{\Delta x}$ is the TKE dissipation using second-order central difference approximation applied to the PIV data. Similarly, $\varepsilon_m|_{2\Delta x}$ is the measured dissipation rate with double grid spacing, $(2\Delta x)$. In other words, the measured dissipation rate is corrected by using PIV measurements with two different spatial resolutions similar to Richardson extrapolation (Ferziger 1981). The turbulence is not homogeneous over the entire chamber, so it is not possible to compare the measured-dissipation rate with the power supplied by the woofers.

2.2. *Particle characteristics*

Three types of particles were used: 500 μm diameter glass, 250 μm glass and 250 μm polystyrene particles. They were all manufactured by U.S.F. Surface Preparation Group. A particle Reynolds number, Re_p, is estimated by using an estimated particle terminal velocity, v_t, and an estimated particle relaxation time, τ_p, as

$$Re_p = \frac{d_p v_t}{\nu}, \tag{2.4}$$

$$v_t = g\tau_p, \tag{2.5}$$

$$\tau_p = \frac{d_p^2}{18\nu}\frac{\rho_p}{\rho_f}\frac{1}{1 + 0.15Re_p^{0.687}}. \tag{2.6}$$

The particle characteristics are listed in table 2. In this study, we define Stokes number as

$$St \equiv \frac{\tau_p}{\tau_f}, \tag{2.7}$$

where τ_f denotes the Kolmogorov time scale for the gas-only turbulence. Kolmogorov time scale is defined as

$$\tau_f \equiv \left(\frac{\nu}{\varepsilon}\right)^{1/2}. \tag{2.8}$$

The Stokes number is above 100 for all three particle types.

2.3. *Particle feeding system*

Solid particles were fed from an Accurate Model 302 volumetric screw feeder located on the second floor right above the chamber laboratory. The 25.4 mm feeder helix had a maximum volumetric feed rate of 2.9×10^4 mm^3 s^{-1}. The particles fell through a 176 mm long by 15 mm diameter tube onto a set of five sieves to make the particle distribution uniform. The upper sieve had 1.54 mm diameter wire with 4.75 mm mesh opening, the next three had 1.0 mm diameter wire with 2.36 mm mesh opening and the last (bottom) had 0.94 mm diameter wire with 2.0 mm mesh opening. A 38 mm long honeycomb with 6.4 mm diameter hexagonal cells was installed to reduce horizontal motion caused by the sieves. Particles entered the chamber through a 152 mm diameter 2.5 m long particle chute so that they had reached terminal velocity before passing into the turbulence chamber. The particles fell through the chamber roughly in a 150 mm diameter column underneath the chute and accumulated on the floor of the chamber. Therefore, the particle mass loading was statistically uniform around the centre of the chamber, but had much lower particle concentration outside of the 150 mm column. All measurements were acquired in a small volume at the centre of the apparatus, well removed from any particle concentration gradients.

2.4. *Particle mass loading ratio*

The mass loading ratio, ϕ, usually is defined as the ratio of particulate and carrier phase mass fluxes in channel and pipe flow experiments, since the total mass flux integrated over the cross-section is relatively easy to measure for internal flows. However, the mass loading measurements for the chamber are different for two reasons. First, the air mass flux cannot be defined because there is no net mean flow. Secondly, the mass loading at the imaged section cannot be obtained from the total particle mass flux through the chamber because the particles are not uniformly distributed across the full chamber width as discussed above. The mass loading ratio has to be measured locally for the region of interest. Therefore, mass loading ratio is defined as the ratio of the mass of dispersed particles to the mass of air in the imaged section:

$$\phi \equiv \frac{\phi_v}{(1-\phi_v)}\frac{\rho_p}{\rho_f} = \frac{m^p}{m^f}. \tag{2.9}$$

We calibrated particle mass loading by comparing with reference conditions. The reference mass loading was obtained for a given screw feeder setting by considering m^p and m^f inside a cylindrical control volume that had a height, $H_c(=1\ [\text{sec}] \times v_t)$ and the same radius, r_p, as the particle chute. During the calibration procedures, the synthetic jet actuators were turned off so that we could assume that the particles fell downward without dispersion. The particle mass within the control volume can be measured by measuring the mass of the accumulating particles at the bottom of the chamber with an OMEGA LCAE-6kg load cell. Then, the reference mass loading can be obtained as

$$\phi_{ref} = \frac{\dot{m}^p}{\pi r_p^2 v_t \rho_f}. \tag{2.10}$$

	d_p (μm)	ϕ	ϕ_v	
Glass	500	0.12	5.5×10^{-5}	
		0.19	8.6×10^{-5}	
		0.45	2.0×10^{-4}	
		0.60	2.7×10^{-4}	(speaker off)
Glass	250	0.41	1.8×10^{-4}	
Polystyrene	250	0.41	4.7×10^{-4}	

TABLE 3. Calibrated mass loading ratio.

Next, we measured the mean number of particles in each image, N^p_{ref}, for reference conditions. Since the actual mass loading ratio only depends on the number of particles, N^p, in the imaged section for the chamber flow, it can be written as

$$\phi = \phi_{ref} \frac{\langle N^p \rangle}{N^p_{ref}}. \tag{2.11}$$

The resultant mass loading ratios calibrated in this experiments are listed in table 3. The uncertainty of the mass loading ratios is 19 % for 500 μm glass, 13 % for 250 μm glass and 12 % for 250 μm polystyrene particles.

3. Sub-Kolmogorov resolution particle image velocimetry

3.1. *PIV system overview*

The challenge in designing the PIV system was to obtain spatial resolution significantly smaller than either the Kolmogorov scale or the particle diameter, while leaving all optical components outside of the test chamber. This required a working distance from the camera and laser lenses to the measurement volume of at least 0.25 m. The system acquired two-dimensional velocity fields in a $3.7 \times 4.7\,\text{mm}^2$ region at the centre of the chamber. The top view of the PIV system is shown in figure 3. A TSI PIVCAM 13-8 camera (12 bit, 1024×1280, 6.7 μm pixel array) with a 200 mm micro-Nikkor lens, a C mount adapter and a 130 mm Cosmicar/Pentax extension tube gave a magnification of 1.83 (figure 4). The resolution for each pixel was 3.7 μm, corresponding to a PIV vector spacing of 59 μm using 32×32 pixel interrogation windows with 50 % overlap. A New Wave Research Solo III-15 PIV Nd:YAG laser (energy 50 mJ pulse^{-1} at 532 nm) was pulsed twice at 35 μs time separation. The laser optical lens components including a cylindrical lens and three spherical lenses are listed in table 4. The e^{-2} laser sheet thickness at the centre of the imaged section was 103 μm as measured by traversing a razor blade and power meter. TSI Insight (ver. 3.30) software activated a TSI Laserpulse synchronizer (Model 610034) to control the CCD camera and lasers. Aluminum dioxide particles (0.3 μm) were used as PIV tracer particles. A 305 mm long, 127 mm diameter cylindrical fluidized bed was used as a tracer seeder.

The standard cross-correlation algorithm with three-point Gaussian fitting (Willert & Gharib 1991) was used. Recursive interrogation window offset with 50 % overlap was incorporated in the PIV code, developed by Hasselbrink & Mungal (2001) and Han (2001). The interrogation window size was 32×32 pixels resulting in an array of 59×75 vectors from each image pair. Spurious vectors that had relative displacements larger than a specified threshold (2 pixels in this study) to the eight neighbouring vectors were rejected at each iteration. We also modified Han's code so that we can

Lens no.	Description	Part no.
1	–250 mm f.d. cylindrical lens	Melles Griot 101LCN011/078
2	300 mm f.d. spherical lens	Newport KPX205AR.14
3	175 mm f.d. spherical lens	Newport KPX196AR.14
4	–12.5 mm f.d. spherical lens	Newport KPX028AR.14
5	Round mirror	Melles Griot 02MPQ013/275

TABLE 4. Laser optics.

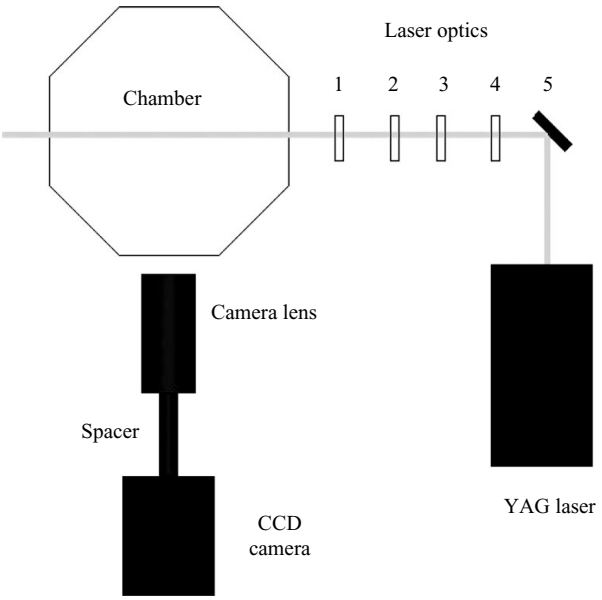

FIGURE 3. Top view of the PIV system. Optical components are listed in table 4.

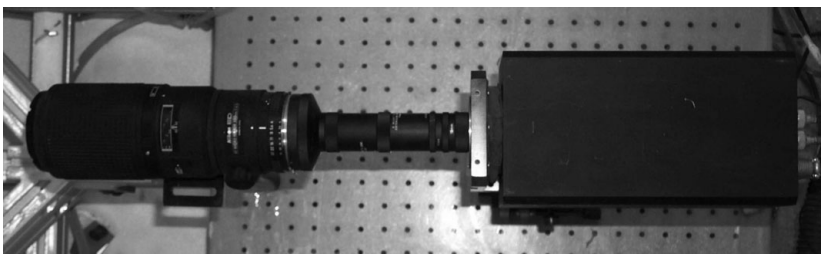

FIGURE 4. PIV camera set-up for high-resolution measurements. TSI's PIVCAM 13-8 camera with a 200 mm micro-Nikkor lens and a C mount adapter and a 130 mm Cosmicar/Pentax extension is used.

check the correlation value of each vector as shown in figure 5. The background colour represents the correlation peak value of each vector. In post-processing, we rejected the vectors with low correlation peaks (less than 0.6), which were probably caused by missing tracers or no tracers in the interrogation window. We used a modified histogram equalization technique (Roth & Katz 2001) to reduce the peak-locking

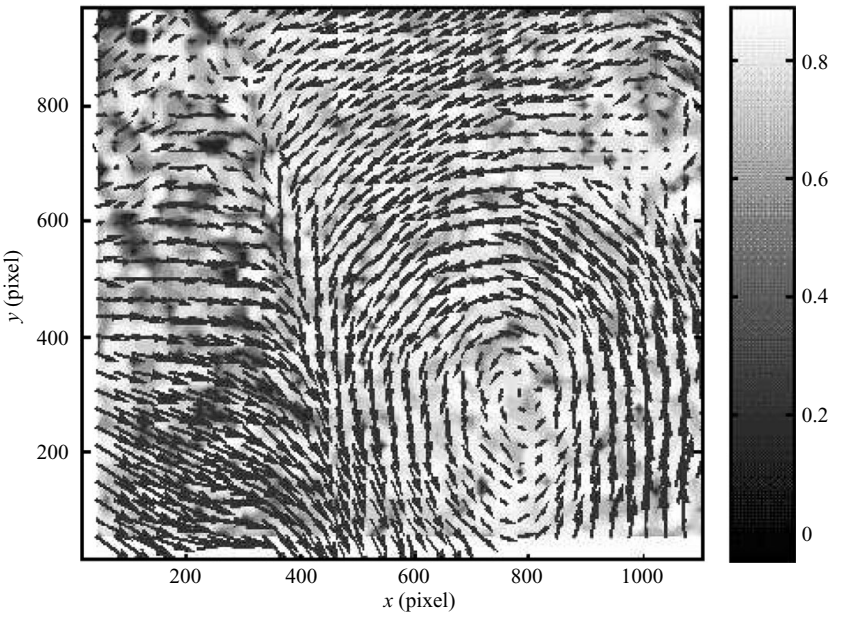

FIGURE 5. PIV vector field with contour plots of correlation peaks.

effects. The uncertainty of the three-point Gaussian fitting is typically expected to be ± 0.2 pixels.

3.2. *Image pre-processing for particle-laden flows*

In order to obtain accurate gas-phase velocity fields, the particulate phase images must be eliminated prior to PIV processing. The present method separated the dispersed particles from tracers by using the difference in image size and intensity after considering two features of the high-resolution measurements. First, the particle diameter is much larger than the tracers, and thus they are not very difficult to discriminate. Secondly, the particle intensity distribution is not Gaussian, since each particle has two bright spots called glare points. Thus, we took a different approach than the previous studies (Hassan *et al.* 1992; Kiger & Pan 2000; Paris & Eaton 2001; Khalitov & Longmire 2002; Hwang & Eaton 2004*b*) because of the high imaging resolution.

After binarizing the images with an intensity threshold of 100 counts brighter than the mean intensity of the image, the bright clusters were labelled using a Matlab labelling function, `bwlabel`. Clusters that had sizes larger than the particle size were considered as particle images and eliminated. Typical original and processed images in the presence of a 250 μm glass particle are shown in figure 6 and similar images with a 500 μm particle are shown in figure 7.

3.3. *Computational resource*

As the spatial resolution improves, the required number of samples increases because the imaged section size becomes smaller. In this study, the two-point velocity correlation between one edge of the field and the other is about 0.8. Thus, almost all velocity vectors in each PIV field are highly correlated. Therefore, more than 40 000 PIV image pairs had to be processed to obtain converged turbulence statistics.

It was not feasible to do all the image processing using the typical laboratory computers, so we developed a unique method to utilize idle time on a large set of

(*a*) Original image. (*b*) Tracer image.

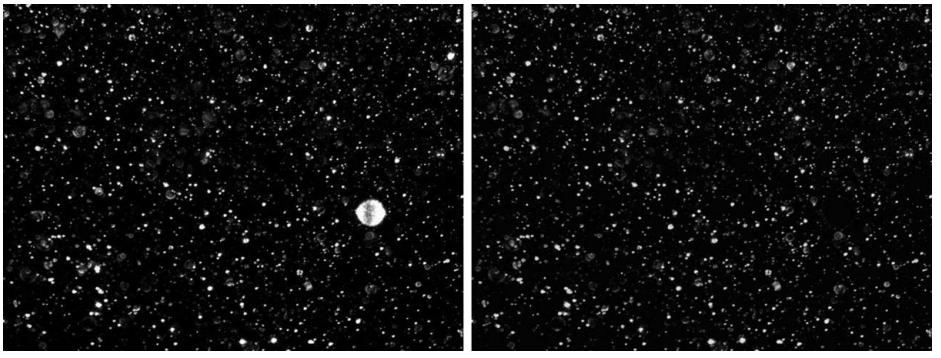

FIGURE 6. Image separation for 250 μm glass particles.

(*a*) Original image. (*b*) Tracer image.

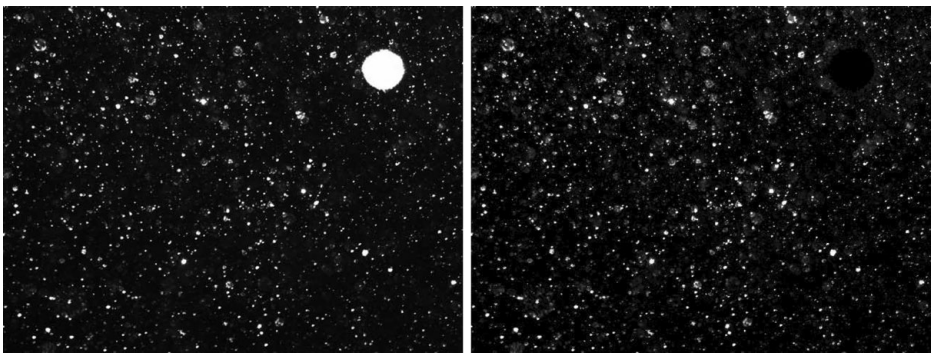

FIGURE 7. Image separation for 500 μm glass particles.

workstations available through the campus network. Details are described by Tanaka & Eaton (2007*b*).

4. Measurements of turbulence modification by particles

4.1. *Overall turbulence modification*

The fluid-phase properties were obtained from between 4500 and 9500 PIV velocity fields (image pairs) for each condition. Figure 8 shows the PDF of the fluctuating fluid velocities in the presence of 500 μm diameter glass particles with (*a*) $\phi = 0.12$, (*b*) $\phi = 0.19$ and (*c*) $\phi = 0.45$. Note that x_1 is the horizontal direction, and x_2 is the vertical direction. The turbulence sampled over the small imaging window is not perfectly isotropic. For the cases of $\phi = 0.12$ and $\phi = 0.19$, the PDF is similar to the unladen case. The corresponding volume fractions are $\phi_v = 5.5 \times 10^{-5}$ and $\phi_v = 8.6 \times 10^{-5}$, which is probably in the one-way coupling regime. For the $\phi = 0.45$ case, the PDF for u_2 is distinctly narrower than the lower loading cases. This indicates that velocity fluctuations in the x_2 direction are attenuated by particles. Similar trends are observed for the 250 μm polystyrene and glass particle cases as shown in figures 9 and 10.

The PDF for the 250 μm glass case is skewed. This indicates that the mean velocity in the x_1 direction for this case is significantly greater than that in the other cases. The mean velocity is due to a secondary flow induced either by the falling particles

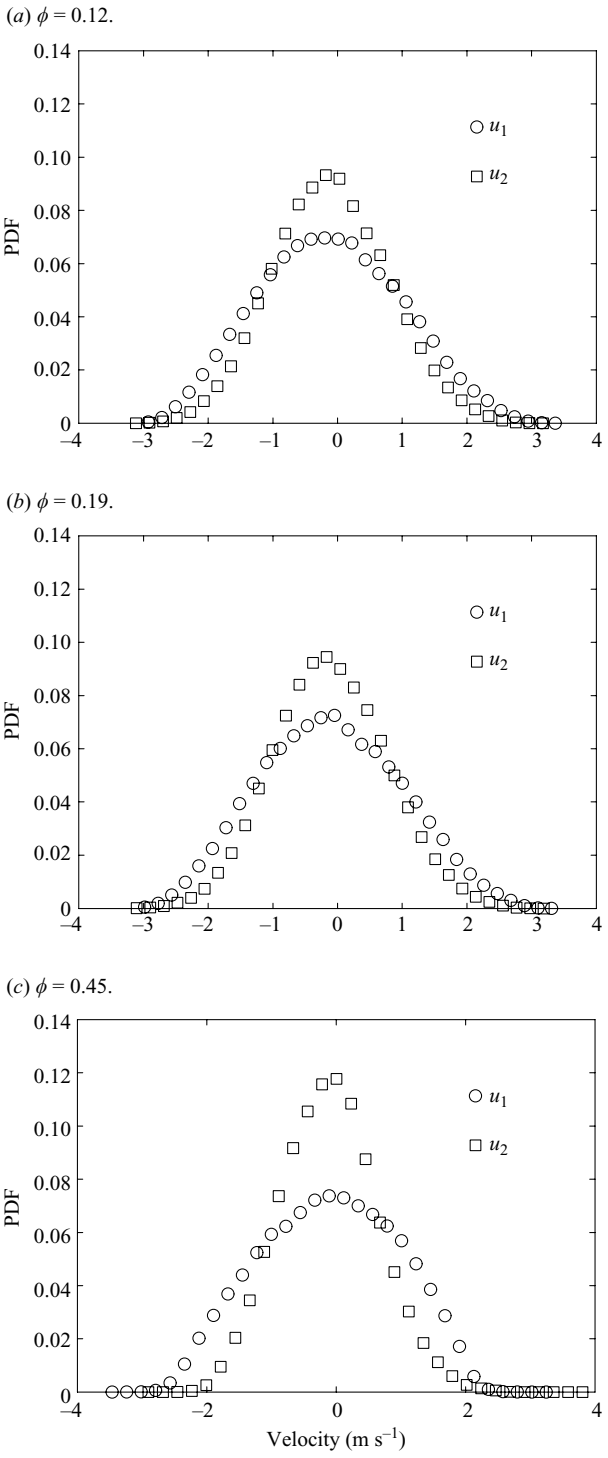

FIGURE 8. Velocity PDFs in the presence of 500 μm glass particles for forced turbulence with $\phi = (a)$ 0.12, (b) 0.19 and (c) 0.45. Circle and square denote u_1 and u_2 velocity components, respectively.

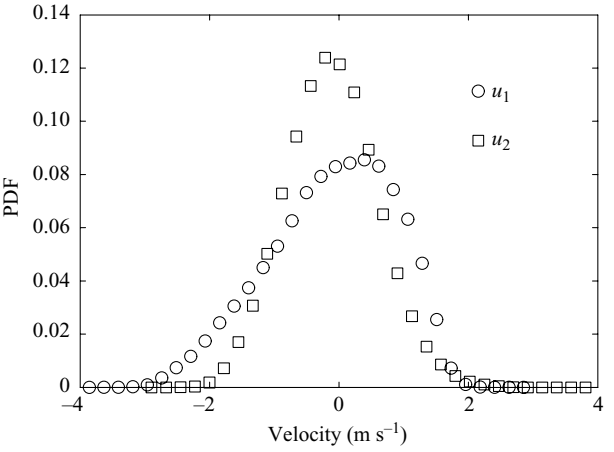

FIGURE 9. Velocity PDFs in the presence of 250 μm glass particles for forced turbulence with $\phi = 0.41$. Circle and square denote u_1 and u_2 velocity components, respectively.

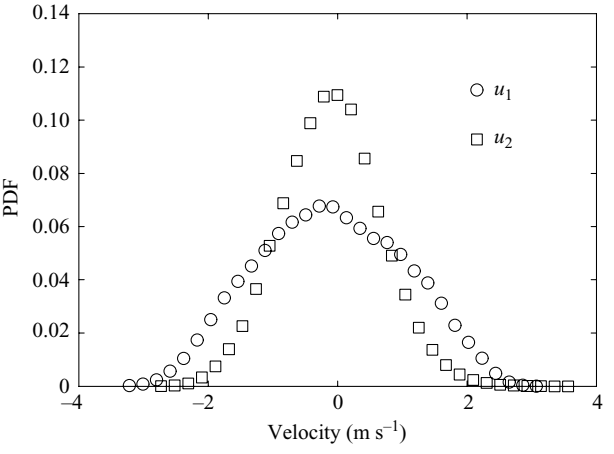

FIGURE 10. Velocity PDFs in the presence of 250 μm polystyrene particles for forced turbulence with $\phi = 0.41$. Circle and square denote u_1 and u_2 velocity components, respectively.

or by asymmetry of the chamber. As the particles fall, they accumulate in a pile at the bottom of the chamber effectively modifying the chamber geometry. The sample domain is a very small volume at the centre of the chamber. Small changes in the chamber geometry might cause the secondary flow pattern to shift relative to the sample domain causing the larger measured mean velocity. Even for this outlying case, the gas-phase mean velocity is just under 1/2 the value of the RMS gas velocity and the particle terminal velocity. This is at least 1 order of magnitude smaller than previous experiments.

An additional case in which 500 μm glass particles were dropped through the flow with the forcing speakers turned off was examined as a baseline. Figure 11 shows the velocity PDFs for this case plotted on the same scale as the forced flow cases. Clearly, the gas phase velocity fluctuations are much smaller than the forced turbulence. The measured gas phase velocity fluctuations are due to turbulence produced by the velocity gradients in the secondary flow and randomly superimposed laminar wakes

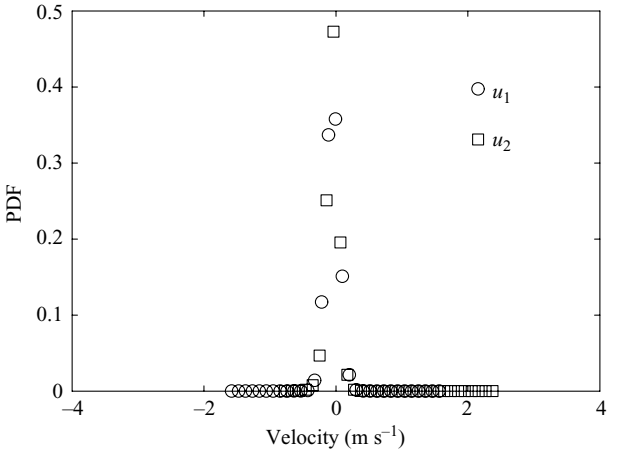

FIGURE 11. Velocity PDFs in the presence of 500 μm glass particles for particle-induced turbulence with $\phi = 0.60$. Circle and square denote u_1 and u_2 velocity components, respectively.

of the particles. Clearly, these sources make a negligible contribution to the turbulence in the forced cases.

Figures 12(*a*) and 12(*b*) show the two components of the mean gas-phase velocity in the presence of particles as a function of mass loading ϕ. For the unladen case ($\phi = 0$), the mean velocity is relatively small; however, as the particle mass loading increases, the mean velocities have greater non-zero values due to mean momentum transfer from the particles. For mass loading around 0.4, the vertical mean velocities, $\langle U_2 \rangle$, are relatively large negative values, which shows that downward flows were induced in the centre of the chamber by the falling particles.

The RMS fluctuating velocities, $\langle u_1^2 \rangle^{1/2}$ and $\langle u_2^2 \rangle^{1/2}$, are presented in figure 13. In the presence of the 500 μm glass particles with $\phi = 0.12$ and $\phi = 0.19$, the RMS velocities are hardly affected by particles in either the x_1 or x_2 directions. These data show that the flow is in the one-way coupling regime at this loading. For the 500 μm glass case with $\phi = 0.45$, the RMS velocity in the x_2 direction was more attenuated than that in the x_1 direction. A similar trend is observed for the 250 μm glass and polystyrene cases. The degree of turbulence attenuation is smaller than the channel flow experiments by Kulick *et al.* (1994) and Paris & Eaton (2001). This may be due to differences in the way turbulence is produced and transported in the flows. Channel flow turbulence is generated by the mean flow strain and transported towards the channel centerplane by turbulent diffusion. The RMS velocities are roughly 10 % of the mean flow velocity, so the TKE level is of the order of one hundredth of the mean flow kinetic energy. On the other hand, in the chamber turbulence, the mean flow is smaller than the RMS velocities, and generation by mean flow strain is insignificant. The previous chamber experiments by Hwang & Eaton (2004*b*) showed a similar level of attenuation to the present study. It is interesting to note that the modification of the RMS velocity in the horizontal direction is relatively small, while the experiments by Kulick *et al.* (1994) and Paris & Eaton (2001) showed that the RMS velocities in both the horizontal and the vertical directions were significantly attenuated. This may be caused by the difference of the particle diameters. Kulick *et al.* (1994) used 50 μm and 90 μm glass, Paris & Eaton (2001) used 150 μm glass and Hwang & Eaton (2004*b*) used 165 glass particles, and those particle diameters

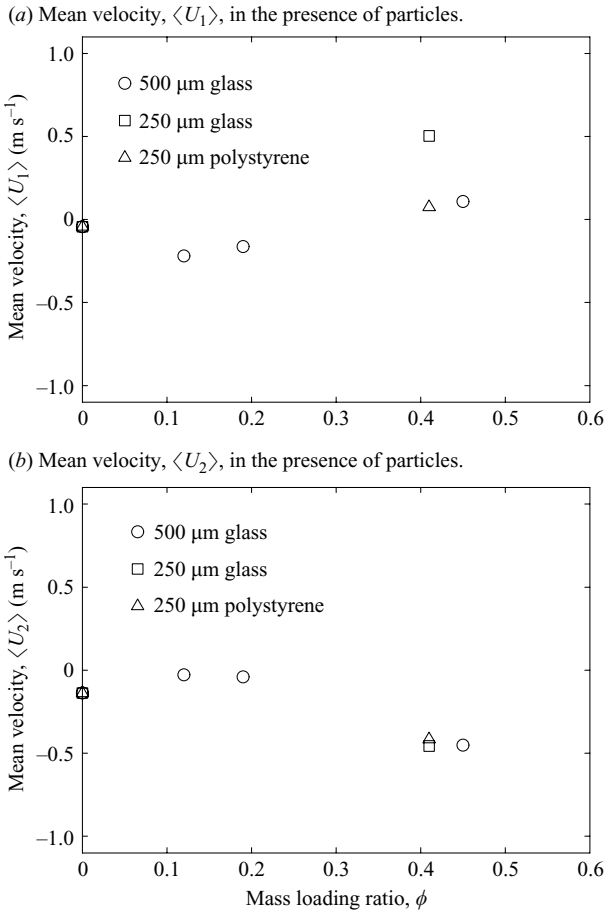

FIGURE 12. Mean velocity, (*a*) $\langle U_1 \rangle$ and (*b*) $\langle U_2 \rangle$, in the presence of particles. Circles show the 500 μm glass case, squares show the 250 μm glass case and triangles show the 250 μm polystyrene particles case.

are smaller than those used in the present experiments by a factor of up to 10. As the particle diameter increases, the augmentation effects may become greater due to the particle wakes, while the attenuation effects are dominant leading to overall attenuation for smaller particles. However, it is difficult to capture those effects, by considering a single dimensional parameter such as diameter. A more comprehensive discussion on this point is presented by Tanaka & Eaton (2008), where a dimensionless parameter describing turbulence attenuation is derived by non-dimensionalization of the Navier–Stokes equations modified for a particle-laden flow.

The two-point velocity correlations of the gas-phase velocity were obtained using the same PIV velocity fields. The correlation calculation excludes any points containing a particle, but uses all other valid fluid velocity measurements. The longitudinal and lateral velocity correlation functions in the x_1 direction are defined as

$$F_{11}(r) = \frac{\langle u_1(x_1, x_2) \cdot u_1(x_1 + r, x_2) \rangle}{\langle u_1^2 \rangle}, \tag{4.1}$$

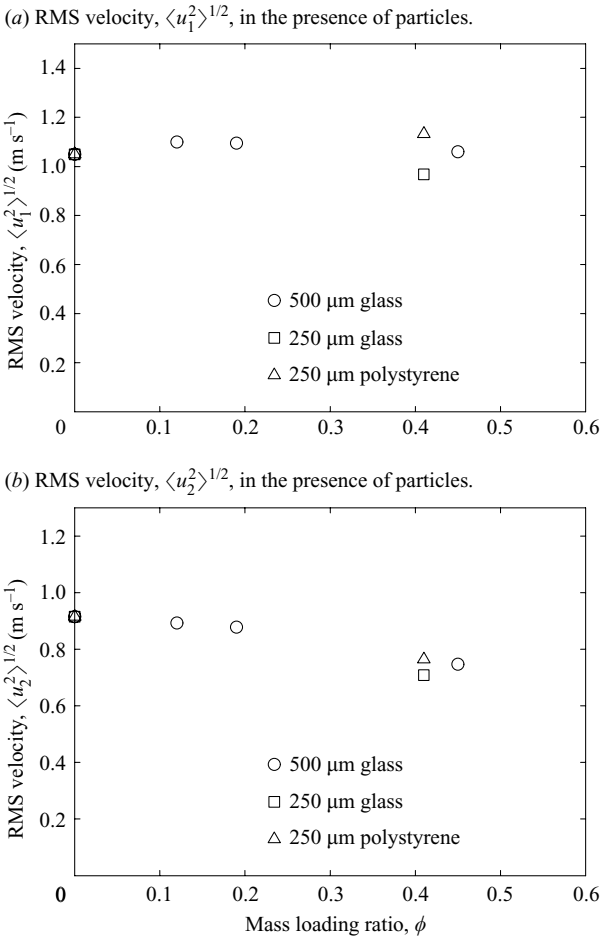

FIGURE 13. RMS velocity, (*a*) $\langle u_1^2 \rangle^{1/2}$ and (*b*) $\langle u_2^2 \rangle^{1/2}$, in the presence of particles. Circles show the 500 μm glass case, squares show the 250 μm glass case and triangles show the 250 μm polystyrene particles case.

$$G_{11}(r) = \frac{\langle u_1(x_1, x_2) \cdot u_1(x_1, x_2 + r) \rangle}{\langle u_1^2 \rangle} \tag{4.2}$$

and $F_{22}(r)$ and $G_{22}(r)$ are defined similarly. The longitudinal two-point correlation functions for the unladen and particle-laden cases are shown in figure 14 and the lateral correlations are shown in figure 15. Note that the correlation coefficient is always greater than 0.6 in those plots. This is because of the high PIV spatial resolution and the resulting small measurement domain size. The largest vector spacing possible for evaluation of the correlation was about 3 mm, significantly shorter than the turbulence integral scale.

The horizontal two-point correlation, F_{11}, slightly decreased with particle loading for all cases except the 250 μm polystyrene particle cases, where F_{11} is almost identical to the unladen case. This coincides with the $\langle u_1^2 \rangle^{1/2}$ measurements, which are not strongly affected by the particles as shown in figure 13. The vertical two-point correlation, F_{22}, significantly decreased regardless of the particle characteristics. The lateral two-point correlation of the u_1 component, G_{11}, is close to the unladen case

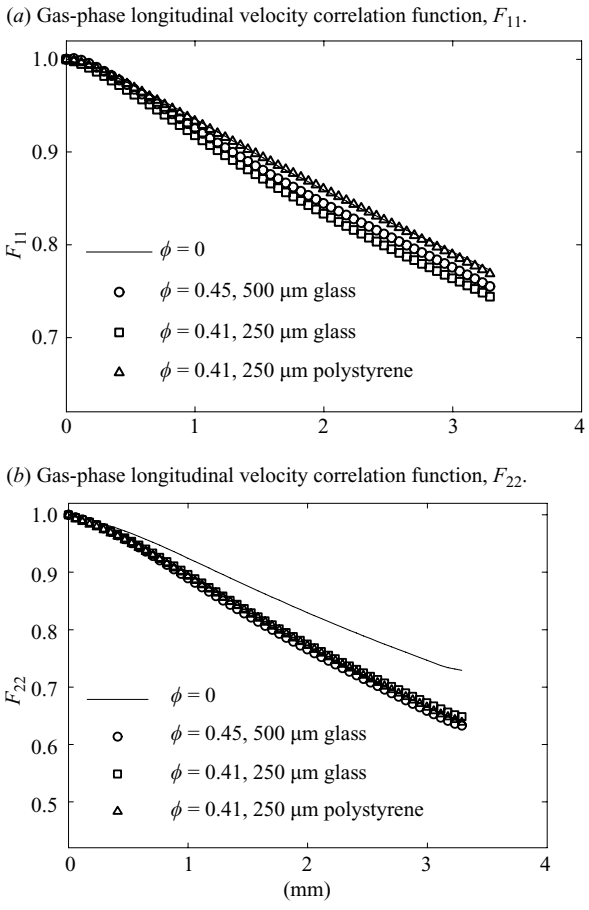

FIGURE 14. Gas-phase longitudinal velocity correlation function: (*a*) F_{11} and (*b*) F_{22}. Circles show the 500 μm glass case, squares show the 250 μm glass case and triangles show the 250 μm polystyrene particles case.

for both sizes of glass particles, while G_{11} for the 250 μm polystyrene case slightly increases. There is no obvious explanation for this difference, but in general all changes in G_{11} are small. The lateral two-point correlation of the u_2 component, G_{22}, decreases significantly for all types of particles. The reductions of the correlations are caused because particles disturb the small-scale structures. Previous studies by Paris & Eaton (2001) and Hwang & Eaton (2004*b*) showed that the two-point correlations for cases with TKE attenuation increased in the presence of the particles for large separation r, while they decreased or stayed almost identical to the unladen case for small r ($r/\eta < 20$). These results indicate that the particles attenuate the large-scale fluid fluctuating velocities, while disturbing small-scale turbulence. Overall, the present results follow these trends for the small-scale turbulence structure.

4.2. *TKE modification*

Figure 16 shows the turbulent kinetic energy modification in the presence of particles, where the TKE was defined in (2.1). The degree of attenuation increases as the mass loading, ϕ, increases. The degree of the TKE attenuation depends upon the particle types even though the mass loading ratio is approximately the same ($\phi \approx 0.4$). The

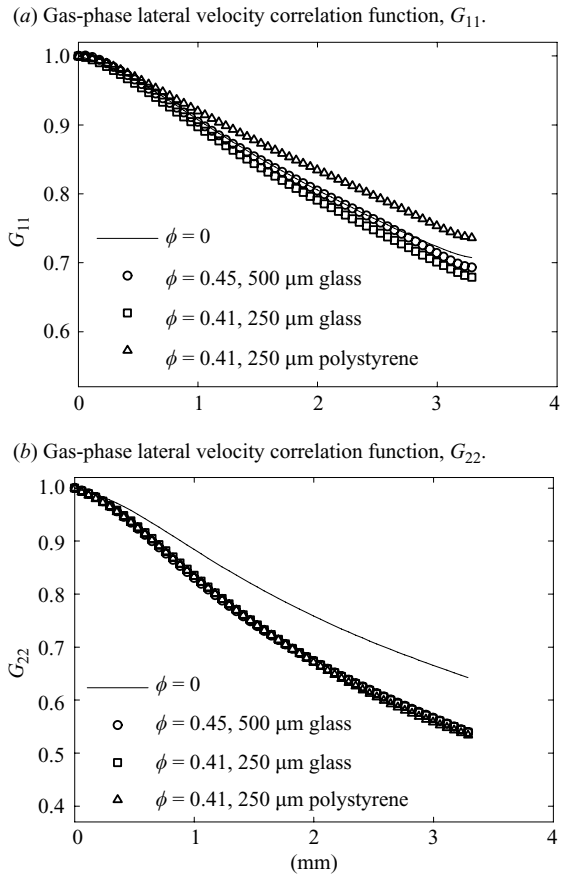

FIGURE 15. Gas-phase lateral velocity correlation function: (*a*) F_{11} and (*b*) F_{22}. Circles show the 500 μm glass case, squares show the 250 μm glass case and triangles show the 250 μm polystyrene particles case.

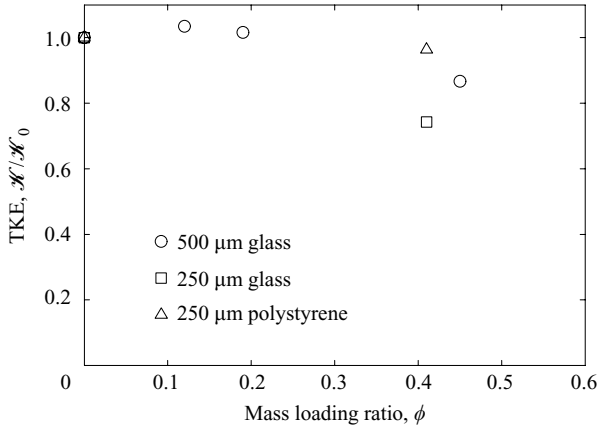

FIGURE 16. TKE modification, $\mathscr{K}/\mathscr{K}_0$, as a function of mass loading, ϕ. Circles show the 500 μm glass case, squares show the 250 μm glass case and triangles show the 250 μm polystyrene particles case. TKE for unladen case, $\mathscr{K}_0$, was 1.39 $m^2\,s^{-2}$.

greatest attenuation was observed in the presence of the 250 μm glass particles, which have higher density, smaller particle diameter and intermediate Stokes number of the three particle types tested.

In order to understand how turbulence is affected by changing particle parameters, and to predict the degree of turbulence modification, we propose a simplified model for the TKE modification based on the TKE transport equation:

$$\frac{\mathrm{D}\mathscr{K}}{\mathrm{D}t} + \frac{\partial \mathscr{T}_j}{\partial x_j} = \mathscr{P} - \varepsilon - \mathscr{F}^p, \tag{4.3}$$

where $\mathscr{T}_j$, $\mathscr{P}$ and $\mathscr{F}^p$ are the transport term, the TKE production and additional energy term due to particles, respectively defined as

$$\mathscr{T}_j = \frac{1}{2}\langle u_i u_i u_j \rangle + \frac{\langle u_j p' \rangle}{\rho_f} - 2\nu \langle u_i s_{ij} \rangle, \tag{4.4}$$

$$\mathscr{P} = -\langle u_i u_j \rangle \frac{\partial \langle U_j \rangle}{\partial x_i}, \tag{4.5}$$

$$\varepsilon = 2\nu \langle s_{ij} s_{ij} \rangle, \tag{4.6}$$

$$\mathscr{F}^p = \frac{1}{\rho_f} \langle u_i f_i' \rangle, \tag{4.7}$$

where f_i' is the fluctuating part of the force per unit volume exerted by the fluid onto particles.

First, we compare the TKE transport equation for the particle-laden case to the unladen base case. Since both the unladen and particle-laden cases are considered to be statistically stationary, the TKE equations for these cases are described as

$$0 = \mathscr{G}_0 - \varepsilon_0, \tag{4.8}$$

$$0 = \mathscr{G}_{ss} - \varepsilon_{ss} - \mathscr{F}^p_{ss}, \tag{4.9}$$

where the superscripts 0 and ss denote unladen and statistically stationary particle-laden conditions, and $\mathscr{G}$ represents the combination of the TKE convection, transport and production in (4.3):

$$\mathscr{G} = -\langle U_j \rangle \frac{\partial \mathscr{K}}{\partial x_j} - \frac{\partial \mathscr{T}_j}{\partial x_j} + \mathscr{P}. \tag{4.10}$$

Note that $\mathscr{G}$ behaves like the energy source term in the forced turbulence that balances the dissipation term and extra dissipation due to particles.

It has not proven fruitful to examine each term in (4.8) and (4.9) to understand turbulence modification, because those terms must sum to zero for statistical stationarity. We may gain more insight into the attenuation process by considering the change in the TKE that occurs during the transient readjustment following an impulsive injection of particles.

The TKE transport equation (see (4.3)) is rewritten using the total TKE budget, $\mathscr{J}(t)$, as

$$\frac{\partial \mathscr{K}}{\partial t} = \mathscr{J}(t), \tag{4.11}$$

$$\mathscr{J}(t) \equiv \mathscr{G}(t) - \varepsilon(t) - \mathscr{F}^p(t), \tag{4.12}$$

where each term is a function of time, t, and particles are added at $t = 0$. Note that the ensemble average in this analysis is the spatial average over the entire domain

of interest in the homogeneous flow. Equations (4.8) and (4.9) are interpreted as the initial and steady state conditions for (4.11). The particle force term behaves like a step function, which is zero before the introduction of particles ($t < 0$). Using $\mathscr{J}$, we can also write the initial conditions for before ($t = 0^-$) and after ($t = 0^+$) introducing particles based on (4.8) as

$$\mathscr{J}(0^-) = \mathscr{G}(0^-) - \varepsilon(0^-) - \mathscr{F}^p(0^-) = 0, \tag{4.13}$$

$$\mathscr{J}(0^+) = \mathscr{G}(0^+) - \varepsilon(0^+) - \mathscr{F}^p(0^+). \tag{4.14}$$

Assuming that $\mathscr{G}$ and ε do not change during the introduction of particles ($\mathscr{G}(0^-) = \mathscr{G}(0^+) = \mathscr{G}_0$, $\varepsilon(0^-) = \varepsilon(0^+) = \varepsilon_0$), the total TKE budget, $\mathscr{J}(0^+)$, right after introducing particles is described as

$$\mathscr{J}(0^+) = -\mathscr{F}^p(0^+) \equiv -\mathscr{F}^p_{0^+}. \tag{4.15}$$

Subtracting (4.9) from (4.14) yields

$$\mathscr{F}^p(0^+) = \Delta\mathscr{G}_{ss} - \Delta\varepsilon_{ss} - \Delta\mathscr{F}^p_{ss}, \tag{4.16}$$

where Δ indicates the change between the unladen state at time 0+ and the statistically stationary-laden state. For example $\Delta\mathscr{G}_{ss} = \mathscr{G}_{ss} - \mathscr{G}(0^+)$.

The TKE can be obtained as a function of time by integrating (4.11) in time as

$$\mathscr{K}(t) = \int_0^t \mathscr{J}(t)\,\mathrm{d}t + \mathscr{K}_0. \tag{4.17}$$

Thus, the degree of the TKE modification, $\Delta\mathscr{K}(t)$, is described as

$$\begin{aligned}\Delta\mathscr{K}(t) &\equiv \mathscr{K}(t) - \mathscr{K}_0 \\ &= \int_0^t \mathscr{J}(t)\,\mathrm{d}t.\end{aligned} \tag{4.18}$$

The TKE budget term, $\mathscr{J}$, is equal to $-\mathscr{F}^p_{0^+}$, when particles are introduced, and then it decays to zero ($\mathscr{J}_{ss} = 0$) with time. This may indicate that the excess (non-zero) TKE budget is distributed to each term ($\mathscr{G}$, ε or $\mathscr{F}^p$).

The individual terms making up $\mathscr{J}(t)$ in (4.18) are not known. We assume that $\mathscr{J}(t)$ can be modelled as an exponential decay with a time constant, $\tau_{\mathscr{K}}$, where $\tau_{\mathscr{K}}$ is to be determined:

$$\mathscr{J}(t) = \mathscr{J}(0^+)\,\mathrm{e}^{-t/\tau_{\mathscr{K}}}. \tag{4.19}$$

By integrating (4.19), $\Delta\mathscr{K}$ is written with the initial condition $\Delta\mathscr{K}(0^+) = 0$ as

$$\Delta\mathscr{K}(t) = \tau_{\mathscr{K}}\mathscr{J}(0^+)(1 - \mathrm{e}^{-t/\tau_{\mathscr{K}}}). \tag{4.20}$$

Considering the statistically stationary particle-laden condition when $t \to \infty$, $\Delta\mathscr{K}_{ss}$ is written as

$$\Delta\mathscr{K}_{ss} = \tau_{\mathscr{K}}\mathscr{J}(0^+). \tag{4.21}$$

Finally, the degree of the TKE modification can be estimated using (4.15) as

$$\Delta\mathscr{K}_{ss} \cong -\tau_p\mathscr{F}^p_{0^+}, \tag{4.22}$$

where we assume that $\tau_{\mathscr{K}}$ is approximated as the particle relaxation time constant, τ_p. It is not clear exactly what time constant should be used in this equation. For the large Stokes number particles, the turbulence integral time scale might be more appropriate. However, the particle time constant could be a logical choice because

this is a scale for the amount of time it takes the particles to absorb energy from the turbulence. On the other hand, a large scale time constant of the carrier phase turbulence like $\mathscr{K}/\varepsilon$ might also be appropriate. This question remains open at this time. It may be possible to resolve this question using direct simulations.

The result indicating that the degree of turbulence modification depends only on the initial particle condition is probably not an appropriate conclusion. However, it can be valid, if the particle initial condition $\mathscr{F}^p_{0+}$ is appropriately introduced so that $\mathscr{J}$ decays as an exponential function with the time constant, τ_p. This implies that appropriate estimates for τ_p (or $\tau_{\mathscr{K}}$) and $\mathscr{F}^p_{0+}$ may give an accurate prediction of the degree of TKE modification.

4.3. *TKE dissipation*

Here, we attempt to further understand the turbulence modification by considering the changes in the dissipation rate between the unladen and particle-laden cases. Previous measurements show that the dissipation rate decreases in proportion to the decrease in TKE. This disagrees with intuition that the particles attenuate turbulence by increasing the dissipation rate. For reasons discussed below, we now believe that those previous measurements are flawed.

Before presenting the new measurements, we first extend the previous analysis of the case where particles are introduced impulsively into initially unladen turbulence. As described in (4.16), the initial energy introduction by particles, $\mathscr{F}^p_{0+}$, can be transferred to other terms such as $\mathscr{G}$ and ε as the turbulence evolves towards the new stationary state. We do not have enough information to compute the full temporal evolution, so we consider a simplified condition, where $\mathscr{G}$ (the source term) is not affected by particles and where particles are introduced at close to their stationary conditions. Thus, $\mathscr{F}^p$ hardly changes during the transition process:

$$\Delta\mathscr{G}_{ss} \approx 0, \tag{4.23}$$

$$\Delta\mathscr{F}^p_{ss} \approx 0. \tag{4.24}$$

Thus, (4.16) can be simplified as

$$\mathscr{F}^p_{0+} = -\Delta\varepsilon_{ss}. \tag{4.25}$$

For turbulence attenuation cases, $\mathscr{F}^p_{ss}$ is thought to be positive (Squires & Eaton 1990), indicating that the dissipation rate is likely to decrease in the presence of particles for flows that satisfy (4.23). Using (4.22), the degree of the TKE modification can be estimated as

$$\Delta\mathscr{K}_{ss} = \tau_p \Delta\varepsilon_{ss}. \tag{4.26}$$

By normalizing (4.26), it can be rewritten as

$$\frac{\Delta\mathscr{K}_{ss}}{\mathscr{K}_0} = \beta\frac{\Delta\varepsilon_{ss}}{\varepsilon_0}, \tag{4.27}$$

$$\beta \equiv \tau_p\frac{\varepsilon_0}{\mathscr{K}_0}. \tag{4.28}$$

The derivation of (4.27) relies on a rather extensive set of assumptions. However, it is a simple relationship, and it can be tested directly given measurements of the TKE and dissipation rate.

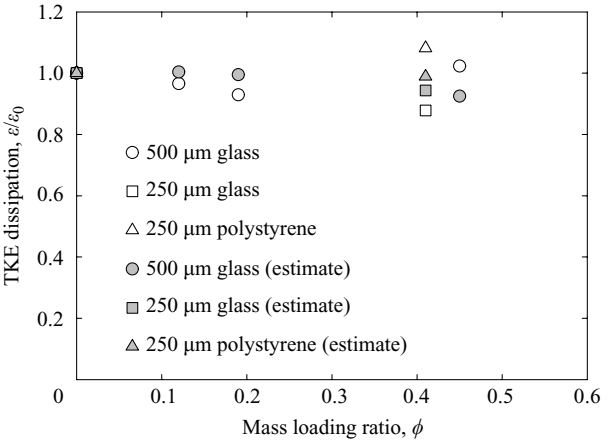

FIGURE 17. Dissipation rate modification, $\varepsilon/\varepsilon_0$, as a function of mass loading, ϕ. Circles show the 500 μm glass case, squares show the 250 μm glass case and triangles show the 250 μm polystyrene particles case. The open symbols are the measured dissipation and filled symbols showed the estimated dissipation based on (4.31). The dissipation rate for unladen case, ε_0, was 28.2 $m^2\,s^{-3}$.

Next, we examine the TKE dissipation rate from the experimental data. The TKE dissipation was calculated as

$$\varepsilon = \frac{3}{2}(\varepsilon_{11} + \varepsilon_{22}) + 6\varepsilon_{12}, \tag{4.29}$$

where each term was obtained using the correction method described in (2.3). Previous dissipation measurements in particle-laden flows by Paris & Eaton (2001) and Hwang & Eaton (2004*b*) showed that the dissipation rate decreased in rough proportion to the turbulent kinetic energy, so

$$\frac{\Delta\varepsilon}{\varepsilon_0} \sim \frac{\Delta\mathscr{K}}{\mathscr{K}_0}. \tag{4.30}$$

As seen in figure 17 (open symbols), the present measurements show that the dissipation changes little with mass loading.This difference is likely due to the inadequate measurement resolution used in the previous experiments. For Paris & Eaton (2001), the inter-vector spacing was greater than the Kolmogorov scale. This likely caused an underestimation of the dissipation rate as described by Tanaka & Eaton (2007*a*). Hwang & Eaton (2004*b*) used the large eddy PIV method proposed by Sheng, Meng & Fox (2000) for the estimate of the dissipation rate. Although this method is one of the most useful for PIV with inter-vector spacing larger than the Kolmogorov scale, its accuracy needs to be discussed because two critical assumptions are used in the method. First, the Smagorinsky model is used to estimate the SGS stress. Thus, the accuracy of the dissipation rate is expected to be similar to LES with the Smagorinsky model. Secondly, all the energy from large to small eddies is assumed to dissipate in the unresolved scales. This is valid if the filter width is in the inertial subrange. This method may underestimate the dissipation rate, if the vector spacing is too large because it does not include the dissipation in the resolved scale, ε_{GS}. For particle-laden flows, the second assumption also requires that the particle term, $\mathscr{F}^p_{SGS}$, be negligible, since this method is constructed for single phase turbulence. In particle-laden flows, the strong strain around particles plays an important role in

TKE energy dissipation, and this cannot be obtained without adequately resolved measurements.

Based on (4.26), the dissipation rate for the particle-laden turbulence can be estimated as

$$\varepsilon_{ss} = \varepsilon_0 + \frac{\Delta \mathscr{K}_{ss}}{\tau_p}. \tag{4.31}$$

The filled symbols in figure 17 show the estimated dissipation based on (4.31). The discrepancies between the measured and the estimated dissipation are within 10 % of the unladen dissipation rate. This indicates that the above analysis captures the trend that the relative changes of the dissipation rate in the presence of particles are smaller than the changes in the TKE.

The small changes in dissipation were roughly what would be expected based on (4.27). The ratios, β, were 7.9 for 500 μm glass, 3.8 for 250 μm glass and 1.9 for 250 μm polystyrene particles, respectively. Therefore, we expect relative dissipation rate modifications, $\Delta\varepsilon_{ss}/\varepsilon_0$, to be smaller than $\Delta\mathscr{K}_{ss}/\mathscr{K}_0$. Thus, the dependence of the dissipation modification on the mass loading ratio is expected to be smaller than that of the TKE modification. For the 500 μm glass particle case, the dissipation modification, $\Delta\varepsilon_{ss}/\varepsilon_0$, is expected to be about one order smaller than $\Delta\mathscr{K}_{ss}/\mathscr{K}_0$. The 250 μm glass case has the greatest attenuation of the dissipation rate due to the greatest TKE attenuation and intermediate β. For the 250 μm polystyrene case, the modification of the dissipation is expected to be small because of the small TKE modification as described in figure 16, though the ratio β is small. The measured dissipation for this case slightly increased, while the estimated dissipation is slightly smaller than the unladen case. This is probably due to the secondary flows or the three dimensionality. Though the uncertainty of the dissipation measurements due to the random error is less than 0.1 $\mathrm{m^2\,s^{-3}}$, the effects of the secondary flows or the three dimensionality could not eliminated. Therefore, we cannot quantitatively discuss this trend. However, the trend that the magnitude of the dissipation modification is smaller than the TKE modification is consistent. This indicates that the analysis is useful in order to roughly estimate the dissipation rate in the presence of particles.

4.4. *Turbulence modification around particles*

Next, we focus on the details of the flow in the immediate vicinity around particles using the high-resolution measurement system to produce a more physical understanding of the turbulence modification. All image pairs that contained particles were selected for special processing. The turbulence fields were translated so the particle was at the centre of the field. The turbulence fields were then averaged to observe the local turbulence modification around the particles. Figure 18 shows plots of the turbulent kinetic energy normalized by the unladen TKE, $\mathscr{K}_0$, for (*a*) 500 μm glass at $\phi = 0.45$, (*b*) 250 μm glass at $\phi = 0.41$, (*c*) 250 μm polystyrene particles at $\phi = 0.41$ and (*d*) 500 μm glass (speaker off).

Figure 18(*a*) shows the distribution of turbulent kinetic energy around the 500 μm glass particles and clearly illustrates how the turbulence is strongly attenuated near the particles. The region of strong reduction extends out to nearly twice the particle radius. The degree of attenuation slowly falls off asymptoting to a value less than 1.0. This indicates an overall reduction in the turbulent kinetic energy throughout the entire flow field. There is a large region beneath the particle where the kinetic energy is 60 % or less of the unladen TKE level. Note that a similar asymmetry is observed

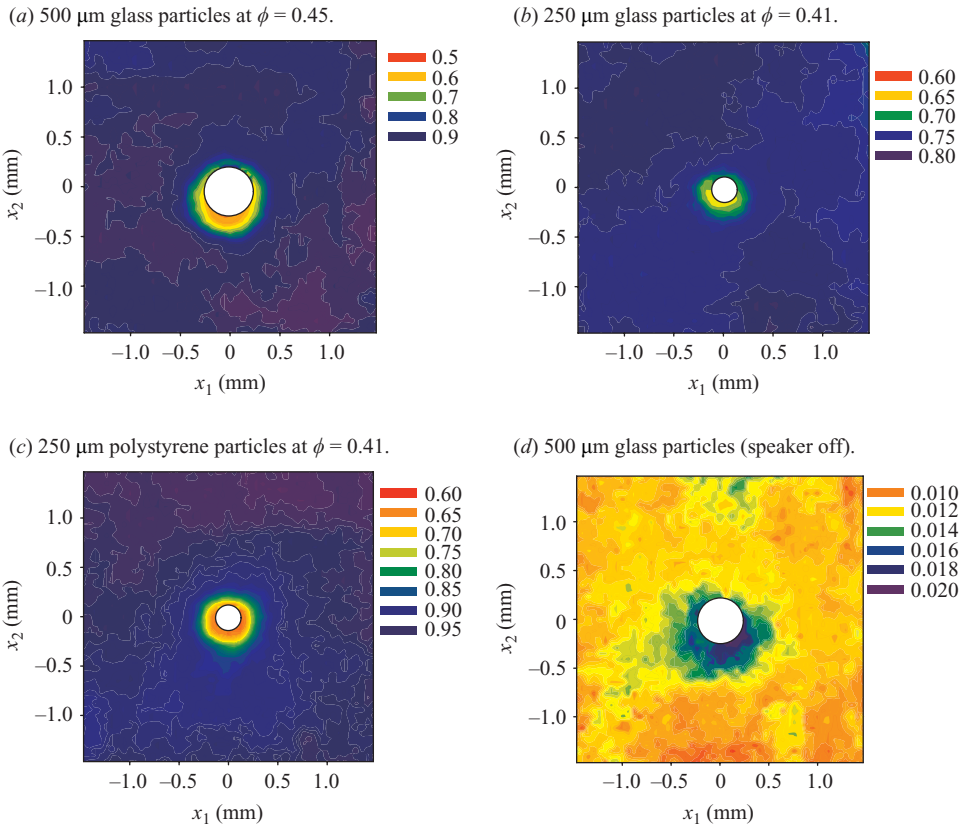

FIGURE 18. Contour plots of TKE around particles, $\mathscr{K}/\mathscr{K}_0$, for (*a*) 500 μm glass at $\phi = 0.45$, (*b*) 250 μm polystyrene particles at $\phi = 0.41$, (*c*) 250 μm glass at $\phi = 0.41$ and (*d*) 500 μm glass (speaker off). The particles are located at the centre. TKE for unladen case, $\mathscr{K}_0$, was 1.39 $\mathrm{m^2\,s^{-2}}$.

for the 250 μm glass and polystyrene beads shown in figures 18(*b*) and 18(*d*). The reason for the asymmetry is unclear, but it must be associated with the fact that in the mean the particles are falling through the turbulence. The reduction of the TKE around 250 μm polystyrene is apparently higher than that of 250 μm glass. This is probably because the entire TKE level for the 250 μm glass particle-laden case is smaller than that for the polystyrene particle-laden case as shown in figure 18.

We believe that the strong local attenuation around each particle is due to the large density difference between the particle and fluid ($\rho_p/\rho_f \sim 10^3$). As in grid turbulence, particles with much larger density than fluid possibly act like grids and attenuate turbulence. These high inertia particles can respond only to the turbulent eddies with the largest time and length scales, and therefore, act essentially as a solid barrier to the turbulence. The no-slip condition on the particle surface affects eddies of all scales, and the impermeability conditions also affects smaller eddies. Thus, we conclude that the particles behave as localized dampers of the turbulence motion. This is essentially the same as the 'screen effect' discussed qualitatively by Hwang & Eaton (2004*b*).

We might have expected that the particles in this size and Reynolds number range might actually augment the turbulence locally, particularly behind the falling particle. Measurements for the case with the forcing turned off in figure 18(*d*) illustrate

turbulent kinetic energy levels around the particle. Note that TKE for this case includes quasi-turbulent kinetic energy, since the particle Reynolds number for the current falling particles is 134, smaller than the critical particle Reynolds number in range from 210 to 270 obtained by numerical studies (Natarajan & Acrivos 1993; Tomboulides & Orszag 2000). Though the TKE levels are about twice the far-field value, the magnitude of the peak turbulence kinetic energy for this case is only about 2 % of the level of the forced unladen turbulence. Therefore, it appears that the local turbulence augmentation around particles may have some effect for this range of particle parameters, but that it is considerably smaller than the screen effect discussed above.

4.5. *TKE dissipation around particles*

The TKE dissipation around particles is calculated by using the forward difference correction method in order to investigate phenomena immediately adjacent to the surface of a particle. The forward difference method is similar to the central difference, and is described as

$$\varepsilon^{(p,q)} \cong \frac{9\varepsilon_m^{(p,q)}\big|_{3\Delta x}^{F} - 4\varepsilon_m^{(p,q)}\big|_{2\Delta x}^{F}}{5},$$

where the superscript, F, denotes the forward difference. Forward differentiation in the radial outward direction was used. Plots of the TKE dissipation around particles are shown in figure 19. Figure 19(a) shows a strong local dissipation around particles with the dissipation of up to 100 ($\mathrm{m^2\,s^{-3}}$), which is three times the mean dissipation rate for unladen flow, ε_0. This trend is also seen in the fully resolved DNS by Burton & Eaton (2005). This strong dissipation is due to the strong viscous shear and local pressure gradient around each particle. Also, the particles induce small-scale fluctuations, which augment the energy dissipation. In figure 19(b), strong energy dissipation can be observed even for particle-induced fluctuation. The magnitude of the dissipation is smaller compared to the figure 19(a), but still quite large. This shows the particles induce and dissipate turbulence, simultaneously. For the 250 μm glass and polystyrene particle case, a similar trend is observed around particles as shown in figures 19(c) and 19(d).

5. Summary

The main objective of this study was to investigate experimentally particle-laden turbulence with emphasis on turbulence around particles. It is hoped that a detailed understanding of the highly localized interaction between particles and turbulence will eventually lead to a full understanding and predictability of global modification of carrier phase turbulence by dispersed particles. Previous studies of particle-laden turbulent flows have shown that a dilute dispersion of fine particles can either augment or attenuate the gas-phase turbulent kinetic energy. However, the underlying physical mechanisms of the turbulence attenuation and augmentation are still not well understood.

In this study, turbulence modification was examined macroscopically and microscopically for simple cases of isotropic turbulence in the presence of the 500 μm glass, 250 μm glass and 250 μm polystyrene particles at the mass loading ratio of up to 0.45. Stationary isotropic turbulence with small mean flow velocities was created in a chamber with eight synthetic jets developed by Hwang & Eaton (2004*b*). The Reynolds number, Re_λ, based on the Taylor micro scale of 1.9 mm was 127 for

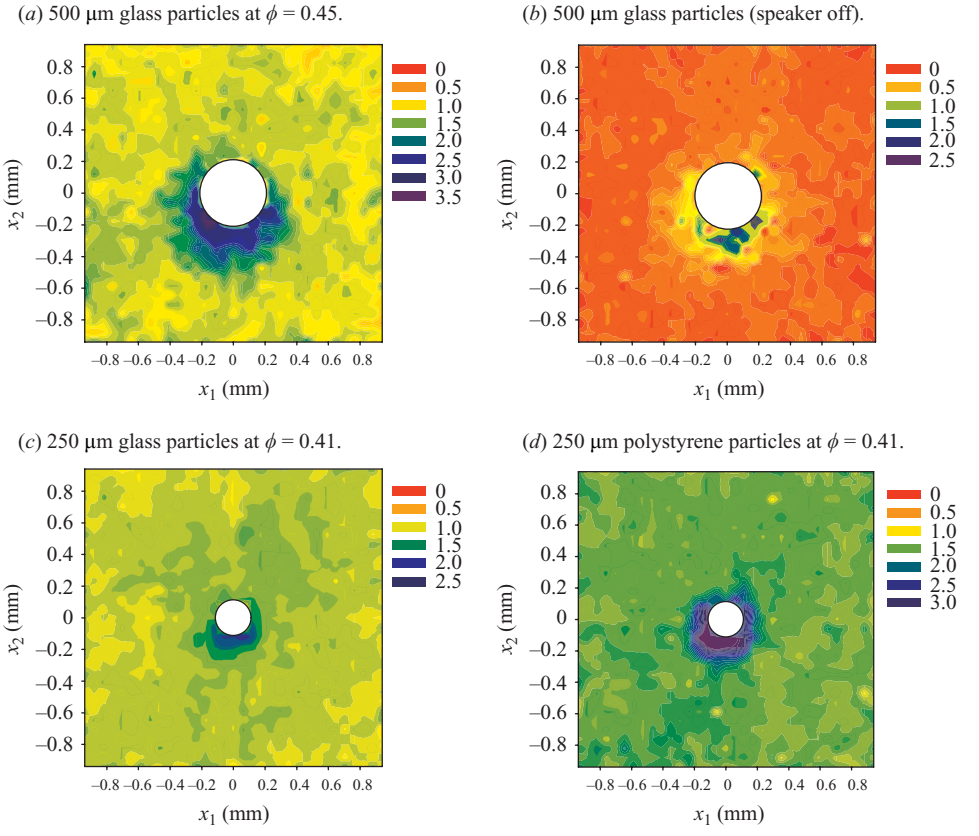

FIGURE 19. Contour plots of TKE dissipation, $\varepsilon/\varepsilon_0$, around particles for (*a*) 500 μm glass at $\phi = 0.45$, (*b*) 500 μm glass (speaker off), (*c*) 250 μm glass at $\phi = 0.41$ and (*d*) 250 μm polystyrene particles at $\phi = 0.41$. The particles are located at the centre. The dissipation rate for unladen case, ε_0, was 28.2 $m^2\,s^{-3}$.

the unladen case. A high-resolution measurement system including PIV and PTV systems capable of resolving the flow around an individual particle in a laboratory-scale experiment was developed. Also, a new data analysis method was developed to provide accurate measurements of the dissipation rate in particle-laden gas turbulence.

Turbulence modification by up to 25 % was observed in the presence of particles. The particle-laden turbulence was analysed to estimate the degree of the TKE modification using the TKE transport equation. Specifically, we considered the transient process that would occur after impulsive addition of particles to the statistically stationary unladen turbulence. The analysis indicated that the degree of the TKE modification may be estimated knowing the particle aerodynamic time constant and an energy source term due to particles.

Extending that same analysis to the TKE dissipation rate, we concluded that relative changes in the dissipation rate due to the addition of particles should be significantly smaller than the actual TKE changes. This conclusion disagrees with earlier measurements that showed the dissipation level was attenuated to approximately the same degree as the TKE. However, the analysis was validated by the present experiments which showed small changes in the dissipation for all

cases. We believe that the discrepancy in the experimental results is due to inadequate dissipation measurement techniques used in the previous research.

The small changes in dissipation rate give the mistaken impression that there is little effect of turbulence attenuation on the small-scale turbulence. This was studied by examining the two-point correlations and the subgrid-scale TKE for a range of spatial resolutions. Particles caused the two-point correlations to decrease for most cases, which indicated that the small-scale turbulence structures were disturbed by particles.

We believe that these seemingly contradictory findings indicate that there are two different mechanisms active at small scales. First, as large-scale turbulence is attenuated, there is less energy passed down the cascade for small scales to dissipate. However, the local distortion of the turbulence around the heavy particles produces additional small-scale energy and dissipation rate. For the present particle and flow parameters, these two mechanisms roughly balanced at small scales.

Measurements of the TKE modification in the vicinity of particles were obtained using the high-resolution PIV. The TKE was attenuated close to the particles by a factor of about two. The region of strong reduction extends out to about twice the particle diameter. Also, the strong dissipation, which was about three times the dissipation for the unladen case, was observed around particles. This trend is also seen in the fully resolved DNS by Burton & Eaton (2005). The strong attenuation is probably caused by the sufficiently large density difference between fluid and particles, where they cannot follow the turbulence fluctuating velocity. In such particle-laden turbulence regimes, the momentum of these high inertia particles is hardly affected by the fluid motion. Thus, the particles create strong shear stress via the no-slip condition at the particle surface and the impermeability conditions, and cause strong dissipation around particles. Thus, particles act like TKE dampers.

This study was sponsored by the National Aeronautics and Space Administration through grant number NCC3-640.

REFERENCES

Bagchi, P. & Balachandar, S. 2002 Effect of free rotation on the motion of a solid sphere in linear shear flow at moderate *Re*. *Phys. Fluids* **14** (8), 2719–2737.

Bagchi, P. & Balachandar, S. 2004 Response of the wake of an isolated particle to an isotropic turbulent flow. *J. Fluid Mech.* **518**, 95–123.

Benson, M., Tanaka, T. & Eaton, J. K. 2005 The effects of wall roughness on particle velocities in a turbulent channel flow. *ASME J. Fluids Engng* **127**, 250–256.

Boivin, M., Simonin, O. & Squires, K. D. 1998 Direct numerical simulation of turbulence modulation by particles in isotropic turbulence. *J. Fluid Mech.* **375**, 235–263.

Boivin, M., Simonin, O. & Squires, K. D. 2000 On the prediction of gas–solid flows with two-way coupling using large eddy simulation. *Phys. Fluids* **12** (8), 2080–2090.

Burton, T. M. & Eaton, J. K. 2005 Fully resolved simulations of particle–turbulence interaction. *J. Fluid Mech.* **545**, 67–111.

Crowe, C. T., Troutt, T. R. & Chung, J. N. 1996 Numerical models for two-phase turbulent flows. *Ann. Rev. Fluid Mech.* **28**, 11–43.

Druzhinin, O. A. 2001 The influence of particle inertia on the two-way coupling and modification of isotropic turbulence by microparticles. *Phys. Fluids* **13** (12), 3738–3755.

Druzhinin, O. A. & Elghobashi, S. 1999 On the decay rate of isotropic turbulence laden with microparticles. *Phys. Fluids* **11** (3), 602–610.

Eaton, J. K. 2006 Turbulence modulation by particles. In *Multiphase Flow Handbook* (ed. C. T. Crowe), chap. 12, pp. 86–98. Taylor & Francis.

Elghobashi, S. & Truesdell, G. C. 1993 On the two-way interaction between homogeneous turbulence and dispersed solid particles. I. Turbulence modification. *Phys. Fluids* A **5** (7), 1790–1801.

Ferrante, A. & Elghobashi, S. 2003 On the physical mechanisms of two-way coupling in particle-laden isotropic turbulence. *Phys. Fluids* **15** (2), 315–329.

Ferziger, J. H. 1981 *Numerical Methods for Engineering Application*. John Wiley.

Fukagata, K., Zahrat, S., Kondo, S. & Bark, F. H. 2001 Anomalous velocity fluctuations in particulate turbulent channel flow. *Intl J. Multiphase Flow* **27**, 701–719.

Gore, R. A. & Crowe, C. T. 1989 Effect of particle size on modulating turbulence intensity. *Intl J. Multiphase Flow* **15** (2), 279–285.

Han, D. 2001 Study of turbulent nonpremixed jet flames using simultaneous measurements of velocity and CH distribution. *Tech. Rep.* TSD-134. Stanford University.

Hassan, Y. A., Blanchat, T. K., Seeley, C. H. & Canaan, R. E. 1992 Simultaneous velocity measurements of both components of a two-phase flow using particle image velocimetry. *Intl J. Multiphase Flow* **18**, 371–395.

Hasselbrink, E. F. & Mungal, M. G. 2001 Transverse jets and jet flames. Part 2. Velocity and OH field imaging. *J. Fluid Mech.* **443**, 27–68.

Hwang, W. & Eaton, J. K. 2004*a* Creating homogeneous and isotropic turbulence without a mean flow. *Exp. Fluids* **36** (3), 444–454.

Hwang, W. & Eaton, J. K. 2004*b* Modification of homogeneous and isotropic turbulence by solid particles. *Tech. Rep.* TF-90. Stanford University.

Hwang, W. & Eaton, J. K. 2006 Homogeneous and isotropic turbulence modulation by small heavy ($St \sim 50$) particles. *J. Fluid Mech.* **564**, 361–393.

Khalitov, D. A. & Longmire, E. K. 2002 Simultaneous two-phase PIV by two-parameter phase discrimination. *Exp. Fluids* **32** (2), 252–268.

Kiger, K. T. & Pan, C. 2000 PIV technique for the simultaneous measurement of dilute two-phase flows. *J. Fluids Engng* **122**, 811–818.

Kiger, K. T. & Pan, C. 2002 Suspension and turbulence modification effects of solid particulates on a horizontal turbulent channel flow. *J. Turbul.* **3** (19), 1–21.

Kulick, J. D., Fessler, J. R. & Eaton, J. K. 1994 Particle response and turbulence modification in fully developed channel flow. *J. Fluid Mech.* **277**, 109–134.

Kussin, J. & Sommerfeld, M. 2002 Experimental studies on particle behaviour and turbulence modification in horizontal channel flow with different wall roughness. *Exp. Fluids* **33**, 143–159.

Lain, S., Sommerfeld, M. & Kussin, J. 2002 Experimental studies and modelling of four-way coupling in particle-laden horizontal channel flow. *Intl J. Heat Fluid Flow* **23** (5), 647–656.

Lee, S. L. & Durst, F. 1982 On the motion of particles in turbulent duct flows. *Intl J. Multiphase Flow* **8** (2), 125–146.

Ljus, C., Johansson, B. & Almstedt, A. E. 2002 Turbulence modification by particles in a horizontal pipe flow. *Intl J. Multiphase Flow* **28** (7), 1075–1090.

Maeda, M., Hishida, K. & Furutani, T. 1980 Optical measurements of local gas and particle velocity in an upward flowing dilute gas–solids suspension. In *Polyphase Flow and Transport Technology, Century 2–ETC, San Francisco*, pp. 211–216.

Maxey, M. R., Patel, B. K., Chang, E. J. & Wang, L.-P. 1997 Simulations of dispersed turbulent multiphase flow. *Fluid Dyn. Res.* **20**, 143–156.

Natarajan, R. & Acrivos, A. 1993 The instability of the steady flow past spheres and disks. *J. Fluid Mech.* **254**, 323–344.

Paris, A. D. & Eaton, J. K. 2001 Turbulence attenuation in a particle-laden channel flow. *Tech. Rep.* TSD-137. Stanford University.

Roth, G. I. & Katz, J. 2001 Five techniques for increasing the speed and accuracy of PIV interrogation. *Meas. Sci. Technol.* **12**, 238–245.

Saarenrinne, P. & Piirto, M. 2000 Turbulent kinetic energy dissipation rate estimation from PIV vector fields. *Exp. Fluids* Suppl, S300–S307.

Sato, Y. & Hishida, K. 1996 Transport process of turbulence energy in particle-laden turbulent flow. *Intl J. Heat Fluid Flow* **17**, 202–210.

Sato, Y., Hishida, K., Simonin, O. & Squires, K. 2000 On turbulence modulation by particles. In *Proc. 3rd Intl Symp. Turbulence, Heat, and Mass Transfer* (ed. Y. Nagano, K. Hanjalic & T. Tsuji), pp. 939–946.

Segura, J. C., Eaton, J. K. & Oefelein, J. C. 2004 Predictive capabilities of particle-laden large eddy simulation. *Tech. Rep.* TSD-156. Stanford University.

Sheng, J., Meng, H. & Fox, R. O. 2000 A large eddy PIV method for turbulence dissipation rate estimation. *Chem. Engng Sci.* **55**, 4423–4434.

Squires, K. D. & Eaton, J. K. 1990 Particle response and turbulence modification in isotropic turbulence. *Phys. Fluids* A **2** (7), 1191–1203.

Squires, K. D. & Eaton, J. K. 1991 Preferential concentration of particles by turbulence. *Phys. Fluids* A **3**, 1169–1178.

Sundaram, S. & Collins, L. R. 1999 A numerical study on the modulation of isotropic turbulence by suspended particles. *J. Fluid Mech.* **379**, 105–143.

Suzuki, Y., Ikenoya, M. & Kasagi, N. 2000 Simultaneous measurement of fluid and dispersed phases in a particle-laden turbulent channel flow with the aid of 3-D PTV. *Exp. Fluids* **29**, S185–S193.

Tanaka, T. & Eaton, J. K. 2007*a* A correction method for measuring turbulence kinetic energy dissipation rate by PIV validated by random Oseen vortices synthetic image test (ROST). *Exp. Fluids* **42** (6), 893–902.

Tanaka, T. & Eaton, J. K. 2007*b* High resolution measurements of turbulence modification by particles. *Tech. Rep.* TF-102. Stanford University.

Tanaka, T. & Eaton, J. K. 2008 Classification of turbulence modification by dispersed spheres using a novel dimensionless number. *Phy. Rev. Lett.* **101**, 114502.

Tomboulides, A. G. & Orszag, S. A. 2000 Numerical investigation of transitional and weak turbulent flow past a sphere. *J. Fluid Mech.* **416**, 45–73.

Tsuji, Y. & Morikawa, Y. 1982 LDV measurements of an air–solid two-phase flow in a horizontal pipe. *J. Fluid Mech.* **120**, 385–409.

Tsuji, Y., Morikawa, Y. & Shiomi, H. H. 1984 LDV measurements of an air–solid two-phase flow in a vertical pipe. *J. Fluid Mech.* **139**, 417–434.

Willert, C. & Gharib, M. 1991 Digital particle image velocimetry. *Exp. Fluids* **10**, 181–193.

Yamamoto, Y., Potthoff, M., Tanaka, T., Kajishima, T. & Tsuji, Y. 2001 Large-eddy simulation of turbulent gas–particle flow in a vertical channel: effect of considering inter-particle collisions. *J. Fluid Mech.* **442**, 303–334.

Yang, T. S. & Shy, S. S. 2005 Two-way interaction between solid particles and homogeneous air turbulence: particle settling rate and turbulence modification measurements. *J. Fluid Mech.* **526**, 171–216.